



D4.15.3: Report on optimization of morphological image processing approach algorithm results on lidars and ceilometers observations



Deliverable number:	D4.15.3
Work package:	WP4 – Atmosphere
Intermediate Objective:	IO4.6
Deliverable type:	<input checked="" type="checkbox"/> Document, report
	<input type="checkbox"/> Websites, patent filings, videos, etc.
	<input type="checkbox"/> Other: please specify
Dissemination level:	<input checked="" type="checkbox"/> Public
	<input type="checkbox"/> Restricted
Estimated delivery (bimester):	B15
Actual delivery date:	
Author(s) (Partner-OU):	Giuseppe D’Amico, Aldo Amodeo, Davide Amodio, Alberto Arienzo, Francesco Cardelicchio, Pilar Gumà Claramunt, Canio Colangelo, Benedetto De Rosa, Nicola Gianluca Di Fiore, Iliaria Gandolfi, Aldo Giunta, Emilio Lapenna, Teresa Laurita, Simone Lolli, Fabrizio Marra, Michail Mytilinaios, Lucia Mona, Nikolaos Papagiannopoulos, Christina Anna Papanikolaou, Serena Trippetta, Ermann Ripepi, Marco Rosoldi, Donato Summa, Gemine Vivone (CNR-IMAA)
Reviewed by:	Francesco Cairo, Luca Di Liberto (CNR ISAC)
Note:	

IR0000032 – ITINERIS, Italian Integrated Environmental Research Infrastructures System - CUP B53C22002150006 (D.D. n. 130/2022)

Funded by EU - Next Generation EU

Mission 4 “Education and Research” - Component 2: “From research to business” -

Investment 3.1: “Fund for the realisation of an integrated system of research and innovation infrastructures”

Table of contents

1. INTRODUCTION	4
2. MEASUREMENT CAMPAIGN	5
3. MIPA DESCRIPTION	9
4. REFERENCE DATASET	11
5. MIPA VALIDATION/OPTIMIZATION ON HPL	12
6. MIPA VALIDATION/OPTIMIZATION ON LPL	16

Index of figures

Figure 1: Case study 1 (on the left) and 2 (on the right): total attenuated backscatter at 1064 (top row), 532 (middle row) and 355 nm (bottom row) measured by CIAO lidar POLPO. .	7
Figure 2: Case study 1 (on the left) and 2 (on the right): Range Corrected Signal from Lufft – CHM15k (top row), Vaisala – CL51 (middle row) and Vaisala – CL31 (bottom row).	9
Figure 3: MIPA algorithm workflow	10
Figure 4: Case study 1 (on the left) and 2 (on the right): total attenuated backscatter at 1064 (top row), 532 (middle row) and 355 nm (bottom row) measured by CIAO lidar POLPO.	14
Figure 5: Case study 1 (on the left) and 2 (on the right). ABLH retrieved by MIPA on total attenuated backscatter timeseries at 1064 (red curve), 532 (green curve) and 355 nm (blue curve) measured by CIAO lidar POLPO.	15
Figure 6: Case study 1 (on the left) and 2 (on the right)	18
Figure 7: Case study 1 (on the left) and 2 (on the right).	19

Index of tables

Table 1: Instruments involved in the CIAO Atmospheric Boundary Layer Height measurement campaign	6
Table 2: Radiosoundings performed in correspondence with the two considered case studies.	12
Table 3: Optimized MIPA configuration parameters for the three wavelengths of POLPO. (see Sec. 3 for the more detailed parameters description)	13
Table 4: Statistical analysis of the differences with respect to the reference of the ABLH retrieved by MIPA on high-resolution timeseries of the total attenuated backscatter at 1064, 532 and 355 nm for both the case studies considered.	16
Table 5: Optimized MIPA configuration parameters for the three wavelengths of POLPO (see Sec. 3 for the more detailed parameters description)	17
Table 6: reference points	20

1. INTRODUCTION

This deliverable provides a report on the optimization of MIPA (Morphological Image Processing Approach) algorithm¹ for the retrieval of Atmospheric Boundary Layer Height (ABLH) from both High Power Lidar (HPL) and Low Power Lidar (LPL - ceilometer) data. MIPA has been developed at CNR-IMAA in the framework of ACTRIS and it has been evaluated on several HPL observations showing, in general, quite good performance with respect to the traditional ABLH retrieval techniques. The main novelty of MIPA consists in the application of suitable morphological operators on lidar range-resolved timeseries “viewed” as a single 2D image. The usage of suitable structuring elements shape guarantees full exploitation of lidar data for the retrieval of accurate ABLH estimates. Consequently, the ABLHs retrieved by MIPA are quite robust because they rely not only on the vertical dynamic of single lidar profiles, but also on the correlation among contiguous (in time) lidar observations. Additionally, MIPA works mainly on vertical and time correlations of the input dataset, and, consequently, the retrieved ABLHs do not strongly depend on input absolute intensities but on the corresponding relative variations. This feature opens the possibility to extend the applicability of MIPA to many lidar systems (including ceilometers) with different characteristics in terms of Signal-to-Noise Ratio (SNR), detection and acquisition type.

A partial assessment of MIPA on HPLs has been already covered in the deliverable D4.15.2 “Report on the optimization of MIPA algorithm for ABLH determination” where the optimization of MIPA configuration parameters to retrieve accurate ABLHs from HPL observations has been discussed. Data from a dedicated measurement campaign performed at CIAO (CNR-IMAA Atmospheric Observatory) in Spring 2024 have been considered. During the campaign several atmospheric sensors have been operative continuously, including HPLs, LPLs, Doppler lidar, Radar systems, as well as manual and automatic radiosounding systems. Further details about the characteristics of all the instruments involved in the campaign can be found in deliverable D4.15.1 “Report on atmospheric boundary layer height measurement campaign”.

Here we continue the MIPA optimization by evaluating the performance on all the available HPL elastic wavelengths (in the assessment made in D4.15.2 only the 1064 nm wavelength was considered) and, moreover, we evaluate MIPA results obtained from the observations made by three different ceilometers (CHM15k, CL31 and CL51) during the campaign. This investigation is fundamental to provide, through MIPA, standardized ABLHs at continental of global scale by using observations from HPL networks (like for example ACTRIS/EARLINET) and ceilometers network (like for example E-PROFILE).

¹ Vivone, G., D'Amico, G., Summa, D., Lolli, S., Amodeo, A., Bortoli, D., and Pappalardo, G.: **Atmospheric boundary layer height estimation from aerosol lidar: a new approach based on morphological image processing techniques**, *Atmos. Chem. Phys.*, 21, 4249–4265, <https://doi.org/10.5194/acp-21-4249-2021>, 2021

Measurement Campaign

The CIAO ABLH measurement campaign took place at CNR-IMAA (40.60N, 15.72E, 760 m a.s.l.) from 15 April 2024 to 30 June 2024. The main goal is to perform continuous atmospheric remote sensing observations from different types of sensors simultaneously with frequent radiosondes' launches. In this way, a reference dataset for the ABLH retrieval can be established exclusively on the base of temperature and pressure profiles measured by correlative soundings.

Concerning the remote sensing instrumentations, two Doppler radars (MIRA35 and MIRA35C by METEK), a Doppler lidar (Stream Line^{XR} by Halo Photonics), three ceilometers (CL31 and CL51 by VAISALA, CHM15k by Lufft) and a microwave radiometer (RPG-HATPRO-G5 by Radiometer Physics) were operating continuously for the whole campaign period. Moreover, a fixed multi-wavelength Raman lidar, POLPO (POtenza Lidar for Particle Observation), and a mobile and more compact multi-wavelength Raman lidar, M3DUSA (Mobile 3-Depolarization Measurement System for Aerosols)-both by Raymetrics-, operating continuously whenever the atmospheric conditions were suitable for lidar observations (no rain precipitation/low clouds).

Many radiosoundings have been performed (up to 8 launches per day) during selected days of the campaign considered particularly interesting from the atmospheric condition point of view. Such a high launch frequency is a crucial factor for the accurate assessment of MIPA algorithm, as the optimal configuration of MIPA has been found by minimizing the differences of MIPA retrieved ABLHs with respect to the corresponding reference values measured by the soundings. Consequently, the greater the number of reference points, the more accurate the determination of the optimized MIPA configuration. Additionally, the soundings should be intensified in correspondence of ABL transition periods in order to capture the ABL dynamic accurately. CIAO is an ideal site for performing this kind of experiment, as it is equipped with two radiosounding systems (one of which with an automatic launcher and both by VAISALA) which are part of GCOS Reference Upper Air Network (GRUAN). The exact scheduling of the radiosondes' launches has been evaluated case by case based on high-resolution weather model forecasts, with denser launches typically performed in correspondence of ABL transition periods or during special events like dust intrusions.

Additionally, a quite complete set of in-situ instrumentations was operating continuously for the whole campaign period providing useful information for the full characterization of the aerosol at the ground. In particular, data from aethalometer (AE33 by Aerosol Magee Scientific), nephelometer (Aurora 3000 by Acoem), aerodynamic particle sizer (APS 3321 by TSI Incorporated), and PMx samplers are available.

Table 1 summarizes all the instrumentation operative during the campaign.

As already described in deliverable D4.15.2, the following two case studies have been selected:

- **Case study 1:** from 2024-04-28 03:00 UTC up to 2024-05-01 00:00UT
- **Case study 2:** from 2024-04-15 00:00 UTC up to 2024-04-16 12:00UT

The selection has been made to try to meet as much as possible all the conditions ensuring an optimal input dataset for MIPA:

Table 1: Instruments involved in the CIAO Atmospheric Boundary Layer Height measurement campaign

Sensor Type	Instrument	Main Products
HPL	Fixed Multi-wavelength Raman Lidar	Aerosol backscatter @1064, 532 and 355nm Aerosol depolarization ratio @1064, 532 and 355nm
	Mobile Multi-wavelength Raman Lidar	Aerosol extinction @532 and 355nm
	MUSA	Aerosol backscatter @1064, 532 and 355nm Aerosol depolarization ratio @532nm Aerosol extinction @532 and 355nm
Doppler Radar	MIRA36 (35.5GHz)	Doppler spectrum Doppler velocity Linear Depolarization Ratio
	Halo Photonics Stream LineXR (1.5 μm)	Aerosol/cloud backscatter Particles' radial velocity Air masses vertical and horizontal velocity
LPL	CL51 (905nm)	Aerosol backscatter
	CL31 (905nm)	
	CHM15k (1064nm)	Cloud base height
Microwave Radiometer	RPG-HATPRO-G5	Temperature, humidity and cloud liquid water profiles Integrated Precipitable Water Vapour (IPWV) Cloud Liquid Water Path (LWP)
Radiosounding system	MW41 (manual)	Temperature, pressure and humidity profiles
	AS13 (automatic)	
In situ	Aethalometer AE33	Black Carbon (BC) concentration
	Nephelometer Aurora 3000	Particle concentration
	Aerodynamic Particle Size APS 3321	Particle size distribution (0.8-10 μm)
	Condensation Particle Counter (CPC 3750)	Particle number concentration (>10 μm)
	Scanning Mobility Particle Sizer (SMPS 3938)	Size distribution and Concentration (10-800nm)
	ToF-ACSM	Chemical composition and mass (<1 μm)
	PMx samplers	PM10, PM2.5, PM1 concentration

- A) continuous and long as much as possible (ideally with no gaps or with rare and small gaps)
- B) high vertical and time resolution
- C) high/moderate SNR

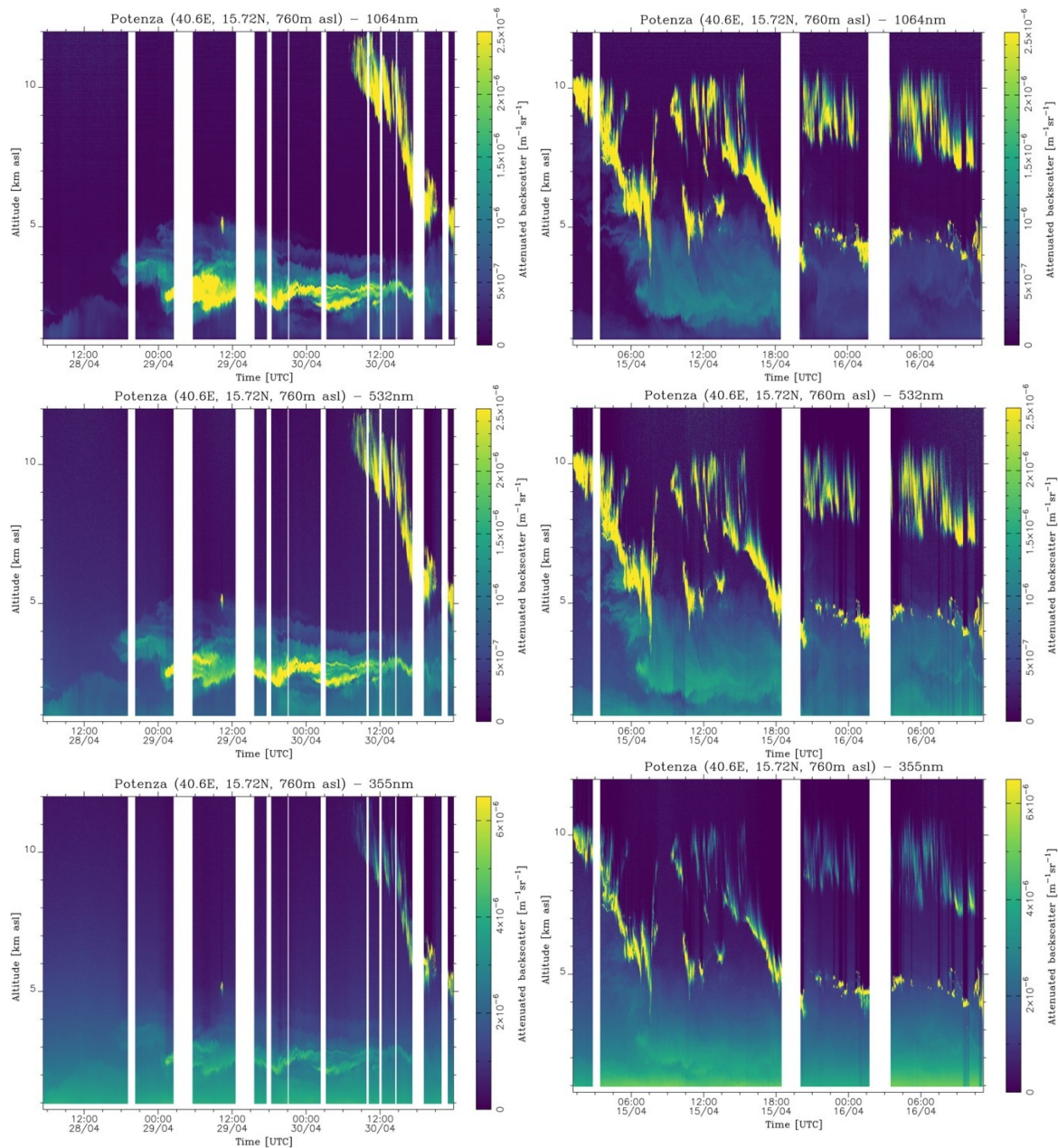


Figure 1: Case study 1 (on the left) and 2 (on the right): total attenuated backscatter at 1064 (top row), 532 (middle row) and 355 nm (bottom row) measured by CIAO lidar POLPO.

Modern HPLs can easily provide a dataset with all these characteristics as they can deliver continuous timeseries of total attenuated backscatter (or even range corrected signal) with time resolution lower than 1-minute, vertical resolution of a few meters, relatively high SNR and at different wavelengths. In general, in HPL signals, the highest contrast between particle and molecular backscattered signal is achieved at the longest available wavelength, typically 1064 nm. Accordingly, the longest available wavelength is theoretically the most suitable for retrieving ABLH, using aerosols as tracers of the atmospheric boundary layer. However, some lidars operate only in visible or UV. To evaluate MIPA's performance at wavelengths other than 1064 nm, we analyzed timeseries of total attenuated backscatter measured by POLPO at all available elastic wavelengths: 355, 532 and 1064 nm. The

optimal MIPA configuration for each wavelength was identified as the one that minimizes discrepancies with respect to the reference points in both case studies.

POLPO timeseries ingested as input by MIPA are shown in Fig.1 for case study 1 (left column) and case study 2 (right column). The total attenuated backscatter timeseries has been delivered by the Single Calculus Chain (SCC), the standard and quality assurance tool for the automatic processing of raw data of ACTRIS aerosol remote sensing observations. POLPO is a multiwavelength Raman lidar capable to measure particle backscatter coefficient and particle depolarization ratio at 355, 532 and 1064nm and particle extinction coefficient at 355 and 532nm. With such set of information, it is possible to fully characterize the atmospheric aerosols in terms of their size, type and shape. An example on how to perform this characterization can be found in the deliverable D4.15.2 where the optical retrieved intensive and extensive particle properties are described for both case studies.

All the measurement gaps (white strips in the figure) are due to internal calibration cycles (mainly dark measurements), switch from daytime to nighttime lidar configuration (or the other way around), and small instrumental issues.

The Range Corrected Signal (RCS) timeseries measured by the three CIAO ceilometers for the case study 1 and 2 are shown in Fig. 2.

By comparing Figs. 1 and 2, the advantages and disadvantages of considering HPL observations instead of the corresponding LPL ones are clearly visible. Typically, the SNR is much better for HPL as in general much more intense laser pulses are used to probe the atmosphere. In particular, the SNR characterizing the CHM15k and CL51 timeseries is still high enough to see the major details of atmospheric aerosol layer while for the CL31 (the ceilometer using the lowest laser power) the decreasing of SNR starts to hide portions of aerosol layer dynamics in both case studies. Consequently, in general, less accurate ABLH estimates are expected when the LPL measurements are considered. On the other hand, ceilometer timeseries do not show any gap and usually are characterized by a lower full overlap height with respect to the HPLs as they usually use smaller telescopes to collect the backscattered light and different geometrical set-ups characterized by larger Field of View (FOV).

A detailed characterization of the atmospheric conditions occurring during both case studies 1 and 2 can be found in the deliverable D4.15.2. Here we briefly recall only the major features.

For case study 1, the typical diurnal evolution of the ABL is affected by the above descending dust layer. During the first two days (28 and 29 April) the impact of the dust layer on the ABL evolution is minimal and the aerosols within the ABL show different optical properties with respect to the dust one (indicating no or minimal mixing). The presence of gravity waves occurring on 30 April indicates more interaction between ABL and dust layer through convective pushing up (due to solar activity) and pulling down (due to dust gravitational settling). The effect of this interaction is the intrusion of dust within the ABL with a consequent mixing of the dust with local aerosols. This is also confirmed by the in-situ instruments measuring a noticeable increase in particle concentration in both fine and coarse mode on 1 May compared to the previous and subsequent days (see deliverable D4.15.2).

Case study 2 is characterized by an intense dust layer extending very close to the ground. This layer has a compressive effect on the ABL dynamics similar to the one described for the layer observed on 30 April, but much stronger. The presence of the layer does not allow

the ABL to follow the typical diurnal growth and, consequently, it remains confined at heights below 1.5km a.s.l. Additionally, the dust layer intrudes the ABL and reaches the ground right after 12:00 UTC. It is worth noting that during that day, this dust layer was clearly visible on the measurement site, reducing the visibility consistently.

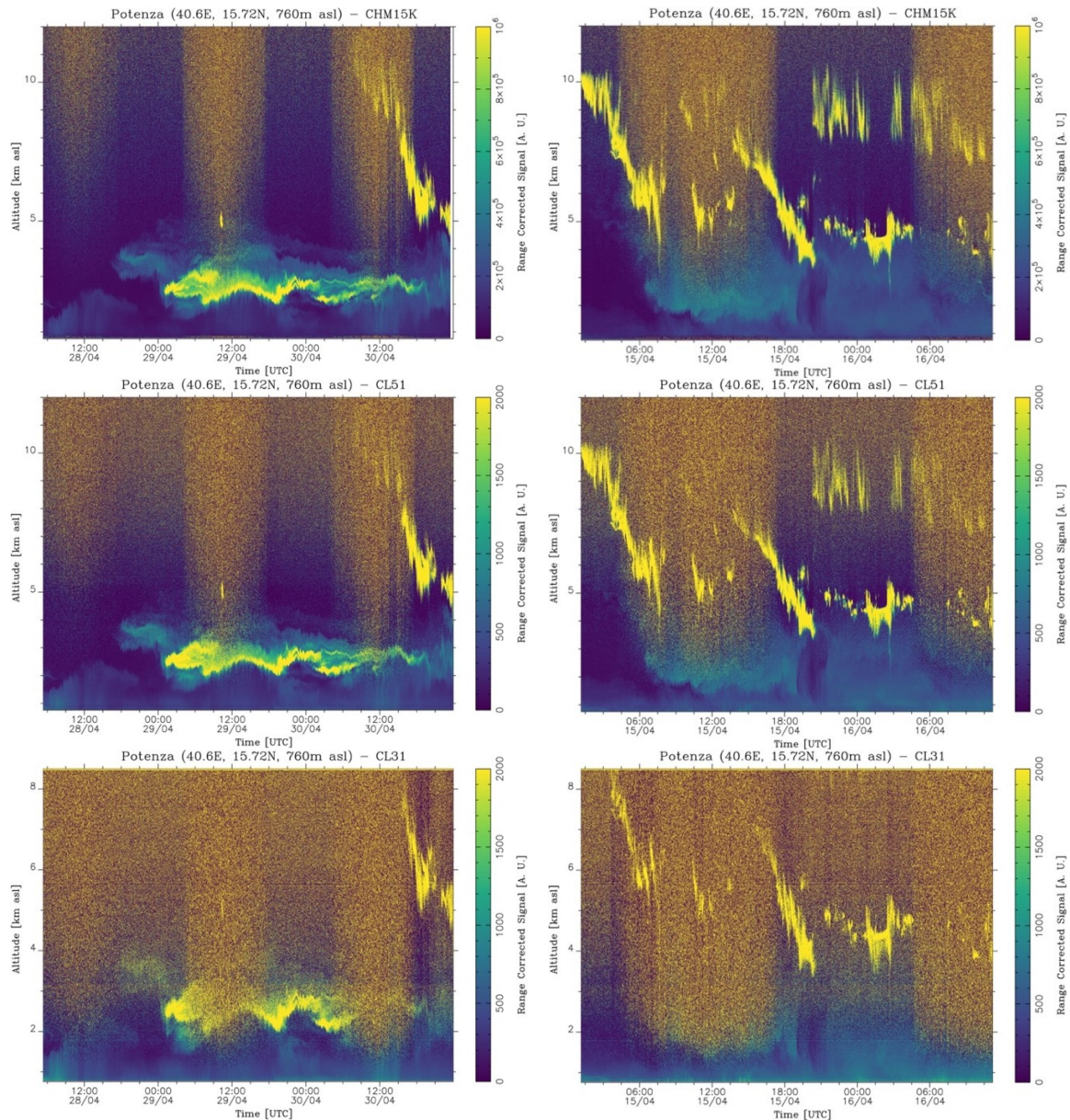


Figure 2: Case study 1 (on the left) and 2 (on the right): Range Corrected Signal from Lufft – CHM15k (top row), Vaisala – CL51 (middle row) and Vaisala – CL31 (bottom row).

2. MIPA DESCRIPTION

The workflow of MIPA algorithm is shown schematically in Fig. 3.

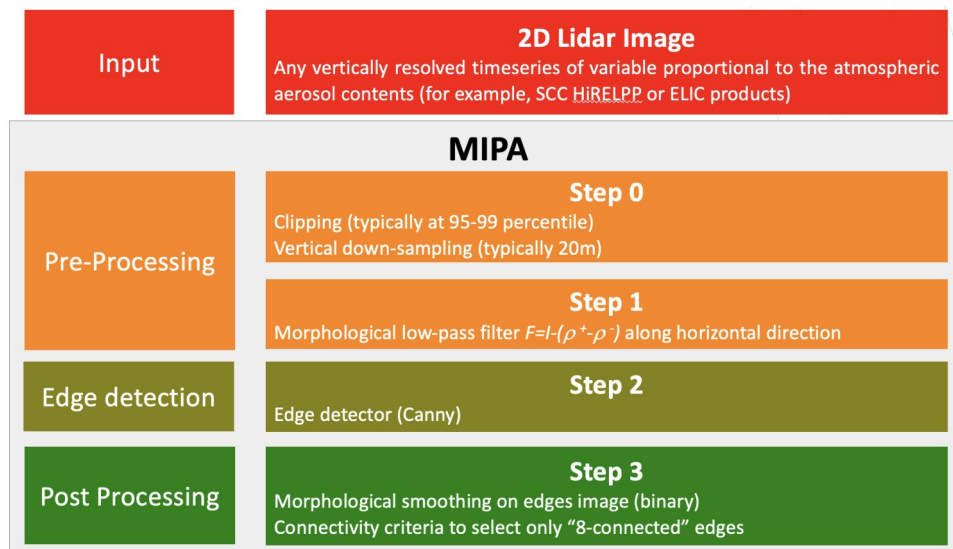


Figure 3: MIPA algorithm workflow

The 2D image on which MIPA is applied consists in the temporal sequence of vertically resolved total attenuated backscatter lidar profiles. Thus, it is a matrix where the number of rows is related to the maximum height and the spatial resolution of the system, whereas the number of columns is related to its temporal resolution and acquisition hours. Firstly, the intensity range of the input image is compressed by applying a clipping operation using percentiles of P for the upper limit (typically between 95 and 99), followed by normalization to scale the values between 0 and 1. This step optimizes the input image's dynamic range by clipping very intense edges (typically coming from clouds). Next, a downsampling operation with a factor R is performed to reduce the spatial resolution of the bins by applying a low-pass filter—a simple sliding average filter of length R . After downsampling, the spatial resolution is no finer than 20 m. This value is chosen to avoid multiple edges corresponding to the same layer, thereby producing sharper and uniquely identifiable edges. In this way we ensure that the edges connected to the aerosol layers (i.e. the ones identifying possible ABLH candidates) fall in region selected by the two threshold values used in Canny edge detection procedure.

After these two preliminary operations (reported as Step 0 in Fig. 3), a pre-processing step is performed (Step 1), where a low-pass morphological filter based on half gradients ρ^+ and ρ^- in Fig. 3) is applied. Such filter corresponds to the semi-sum of special operators called dilation and erosion². This operator is used in the pre-processing phase assuming as structuring element a horizontal line (i.e., along the time direction) with length R . It enables to smooth the lidar image along the horizontal axis (where the dynamics of the ABL are quite slow), directionally reducing the noise and preserving the vertical edges that will be of crucial importance for the next steps.

Afterwards, an edge detector is applied to the pre-processed image. We employed Canny's edge detector (the classical version available in commercial software as MATLAB) to get the first (coarse) estimation of the edge map. The two thresholds defined in the Canny

² Soille, P.: **Morphological Image Analysis: Principles and Applications**, Springer-Verlag, Berlin, Heidelberg, 2003.

algorithm have been kept to the default ones ($th_h=0.7$ $th_l=0.4th_h$). Note that after the clipping operation, each pixel in the image is divided by the maximum value, normalizing the image in the $[0, 1]$ range. The detected edges are indicated with 1; the rest of the map (background) is labeled as 0. All the bins labeled as 1 are potential candidates to represent the ABLH. Finally, the edge map is analyzed by using the following further signal processing:

- **Morphological filters post-processing.** This processing step is done to remove unrealistic edges (i.e., edges that vary too fast with respect to the dynamics of the ABL). Thus, we apply a series of directional low-pass morphological filters. In particular, the used filters are obtained by sequentially applying an opening and a closing operator² using as structuring element a line with a length l_{post} and an angle θ with respect to horizontal direction. θ ranges from θ_{min} to θ_{max} .
- **Object-based post-processing.** As already mentioned, the detected edges are indicated with 1; instead, the rest of the map (background) is labeled as 0. We work on these edges extracting objects. The main concept is the use of the connectivity in an edge map, i.e., the ways in which the bins labeled as “edge” (which assume value 1 in the edge map) are spatially related to their neighbors. A bin declared as “edge” is said “8-connected” if there exists at least one bin belonging to its 8 neighborhoods, i.e. the adjacent bins in vertical, horizontal and diagonal directions, declared as “edges”, as well. All the bins that are “8-connected” to each other form an object. Thus, several objects, clustering the bins declared as “edges”, are collected and analyzed. An analysis about the spatial variability of these objects is performed. Indeed, if the absolute Euclidean distance between the mean of the heights for each extracted object (using the connectivity procedure explained above) and the related mean calculated on the objects in its neighborhood exceeds a threshold δ_{post} , this object is removed from the solution. Finally, the outcome, i.e., the estimated ABLH, is obtained by linearly interpolating the remaining objects in the edge map.

3. REFERENCE DATASET

As reported in deliverable D4.15.2, we assume as reference the values of ABLH calculated from radiosounding data using the algorithm³ based on both potential temperature and horizontal wind vertical profiles.

Tab. 2 summarizes all ABLH calculated out of all the radiosoundings performed in correspondence with the two considered case studies. The soundings are grouped by day. For each day, the launch time (UTC) and the corresponding ABLH (m a.s.l.) calculated by applying the described algorithm are reported. Consequently, Tab. 2 provides the ABLH reference dataset we have used for MIPA optimization/validation.

³ Shuyan Liu and Xin-Zhong Liang, **Observed Diurnal Cycle Climatology of Planetary Boundary Layer Height**, *Journal of Climate*, Vol. 23, 2010, doi: 10.1175/2010JCLI3552.1

Table 2: Radiosoundings performed in correspondence with the two considered case studies.

The soundings are grouped by day. For each day, the launch time (hh:mm UTC) and the corresponding ABLH (m a.s.l.), calculated by applying to the radiosounding datasets the described algorithm⁴, are reported. ABLHs are given in m a.s.l. (measurement site altitude is 760 m).

ABLH reference dataset								
2024-04-15	Time [UTC]		04:18	09:00	12:00	15:00	18:00	21:00
	ABLH [m a.s.l.]		849	1480	1487	1037	1092	892
2024-04-16	Time [UTC]	00:30	04:15	07:54				
	ABLH [m a.s.l.]	812	813	2296				
2024-04-28	Time [UTC]			08:00	13:00	15:30	18:00	21:00
	ABLH [m a.s.l.]			1634	2368	2351	1676	885
2024-04-29	Time [UTC]			08:10	11:00	16:00	19:00	22:00
	ABLH [m a.s.l.]			1537	2205	2232	1244	822
2024-04-30	Time [UTC]	00:45	04:00	08:00	10:59	14:07	17:03	20:00
	ABLH [m a.s.l.]	819	816	1039	2022	1904	2043	1065

4. MIPA VALIDATION/OPTIMIZATION ON HPL

In this section, we discuss how MIPA has been validated and optimized considering the datasets corresponding to the two selected case studies. It is worth noting that the case studies fulfill all the technical requisites for MIPA applicability discussed earlier and, at the same time, they represent a quite challenging dataset to evaluate the performance of MIPA to retrieve accurate ABLH in complex atmospheric scenarios due to the strong dust intrusions characterizing both cases.

To find the optimal MIPA configuration, we have varied all the MIPA configuration parameters and calculated the differences between MIPA retrieved ABLH and the corresponding reference points obtained from the sounding data. We consider optimal the configuration that minimizes the mean square of such differences. This operation has been done for the wavelengths 355, 532 and 1064 nm separately. The corresponding results are summarized in Tab. 3.

As expected, the optimized maximum percentile used for the clipping is very similar for the wavelengths 1064 and 532 nm and a bit higher for the 355 nm. This is a consequence of the decreasing contrast in the lidar signals of the particle to molecular contribution as the wavelength decreases. At 355 nm, where such contrast is the lowest, we need to clip less to get ABLH related edges (i.e. edge coming from aerosol layers) compatible with default Canny thresholds values. As described in Tab. 3, the parameter **P** is the only one for which the corresponding optimized value depends on input wavelength.

Table 3: Optimized MIPA configuration parameters for the three wavelengths of POLPO. (see Sec. 3 for the more detailed parameters description)

Parameter	Description	Optimized value		
		1064 nm	532 nm	355 nm
R	Input image down-sampling factor	6	6	6
P	Clipping maximum percentile	96	95	99
I_{pre}	Length of pre-processing structuring element (horizontal line along the time direction)	3	3	3
I_{post}	Length of post-processing structuring element	4	4	4
θ_{min}	Minimum angle (with respect horizontal direction) of post-processing structuring element	-66°	-66°	-66°
θ_{max}	Maximum angle (with respect horizontal direction) of post-processing structuring element	66°	66°	66°
δ_{post}	Euclidean distance threshold among objects and related neighborhood objects	10	10	10

Fig. 4 shows the ABLH retrieved by MIPA (red curve) when applied to the 1064, 532 and 355 nm timeseries of total attenuated backscatter for the case study 1 (on the left) and 2 (on the right) when the optimal values reported in Tab. 3 are used. Gray dots provide the reference ABLH dataset given in Tab. 2.

In general, for all the wavelengths, during daytime conditions, ABLHs retrieved by MIPA are in good agreement with the reference ones. The expected temporal evolution of the ABL is well captured and the intrusions of the upper dust layers in the ABL do not seem to affect the outcomes, thus obtaining reasonable ABLH estimates.

On the other hand, during nighttime conditions, ABLHs retrieved by MIPA overestimate the reference ones. To explain such behavior, it is important to highlight that MIPA retrieves the ABLH as the top of the first detected aerosol layer. This assumption is valid only if the ABL is above the full overlap height of the lidar performing the measurements. During nighttime observations, this condition is typically not verified, and in this case the algorithm detects as the first edge the base of the layer close to the ABL top. Consequently, the overestimation occurring during nighttime is due to a limitation of the input dataset and not of the algorithm itself, which ideally would have provided ABLH as accurate as in daytime conditions if the lidar measurements had covered regions closer to the ground. The full overlap height for POLPO is 200m a.g.l. for both 355 and 532 nm lidar channels and 400 m a.g.l. for 1064 nm channel.

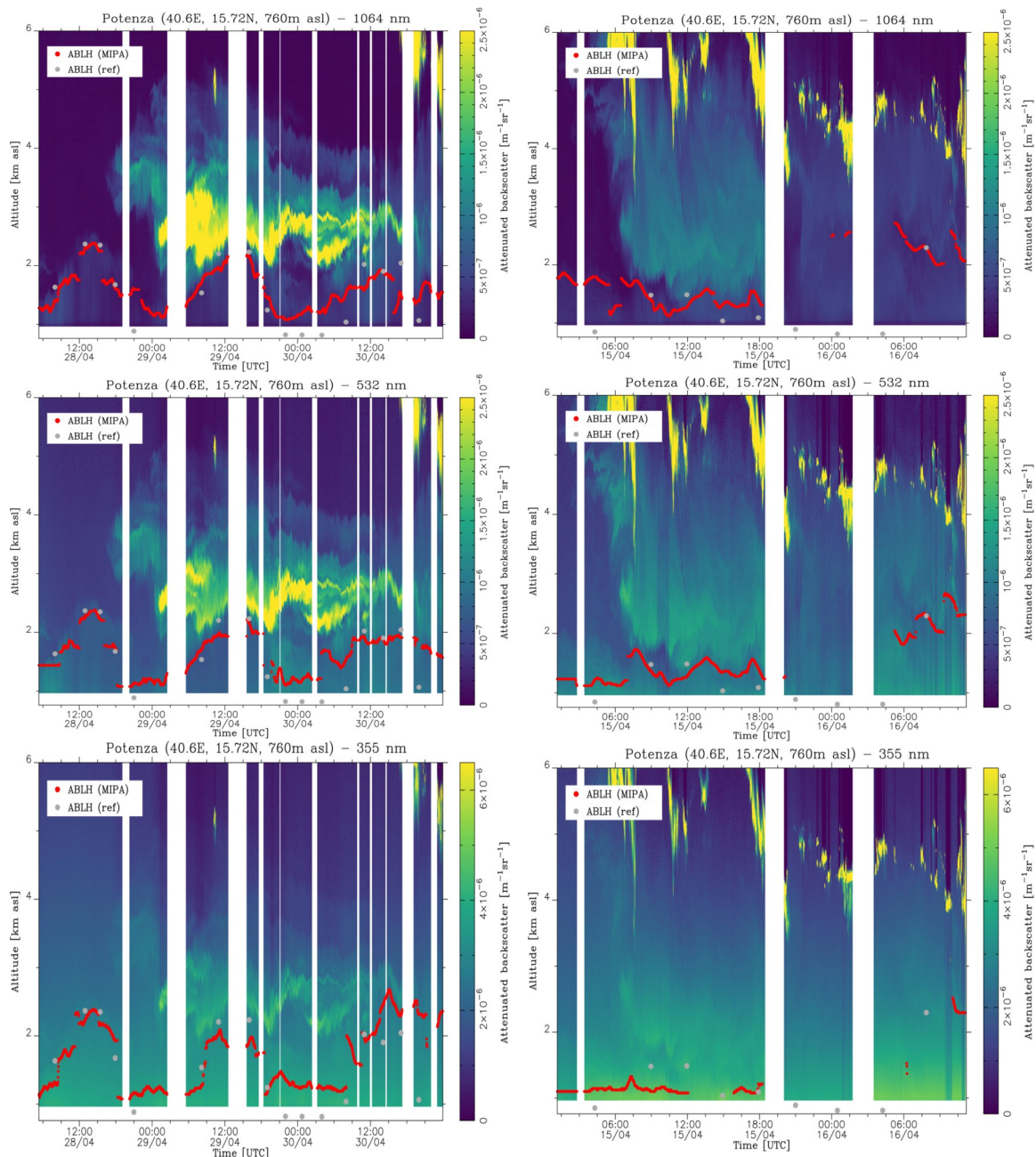


Figure 4: Case study 1 (on the left) and 2 (on the right): total attenuated backscatter at 1064 (top row), 532 (middle row) and 355 nm (bottom row) measured by CIAO lidar POLPO.

The red curve shows the ABLH as retrieved by MIPA while the gray dots are the reference ABLH calculated from radiosoundings.

Additionally, as shown in Fig. 5, the most accurate ABLH estimations are obtained when longer wavelengths are considered. On average, the blue curve in Fig. 5 (corresponding to the shorter wavelength) is the one with larger discrepancies with respect to the reference value indicated by triangles.

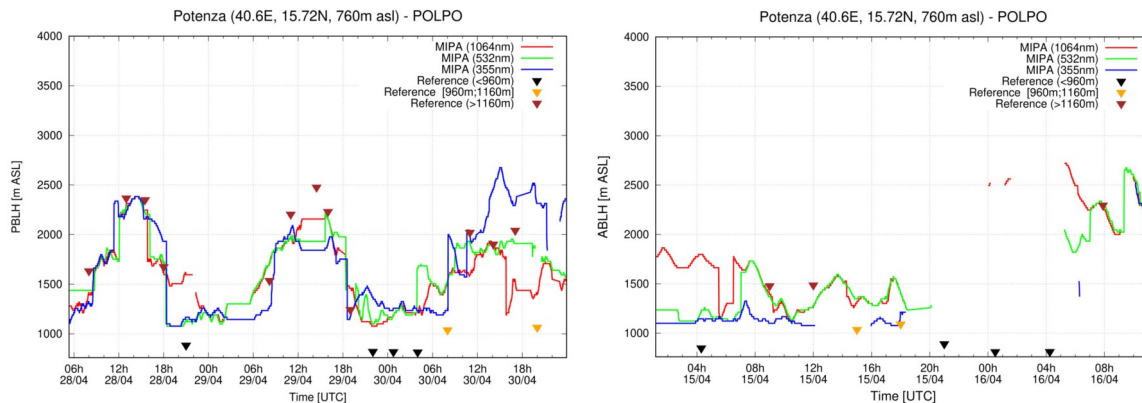


Figure 5: Case study 1 (on the left) and 2 (on the right). ABLH retrieved by MIPA on total attenuated backscatter timeseries at 1064 (red curve), 532 (green curve) and 355 nm (blue curve) measured by CIAO lidar POLPO.

Reference ABLHs calculated from radiosoundings are reported as triangles. Black, orange and brown triangles are reference points below the full overlap of 355 and 532 nm lidar channels, between full overlap heights of green/UV and 1064 nm lidar channels and above full overlap height of 1064 nm lidar channel respectively.

A more quantitative analysis of the differences of ABLHs retrieved by MIPA with respect to the corresponding (in time) reference is given in Tab. 4 considering separately all reference points and only reference points above the full overlap height of the lidar. In Tab. 4 the mean (Δ_{mean}), the median (Δ_{med}), the standard deviation (Δ_{SD}), the standard error (Δ_{SE}), the mean square difference (Δ^2_{mean}), the minimum (Δ_{min}) and the maximum (Δ_{max}) of the differences between ABLH retrieved by MIPA and the corresponding reference points are reported.

When all reference points are considered, the performance of MIPA is quite similar for wavelengths 1064 and 532 nm, while at 355 nm the overall performance is lower.

As already discussed earlier, during nighttime conditions, the input dataset we have used to validate MIPA is not suitable for the detection of ABLH values below the full overlap height of the lidar observations. Consequently, the statistical analysis including all the reference points contains bias due to:

1. inversion algorithm (MIPA)
2. instrumental limitations (ABLH values below lidar overlap height)
3. different ABL definitions (thermodynamic one in case of reference dataset, based on aerosol as ABL tracers in case of lidar dataset)

For a proper MIPA validation discrepancy due to points 2 and 3 should be excluded from the statistical analysis as they both do not apply the specific algorithm used to retrieve ABLH (basically they are present whatever the retrieval algorithm is). To consider only differences due to MIPA, we considered only the reference points above the considered lidar full overlap height (960 m a.g.l. for 355 and 532 nm and 1160m a.g.l. for 1064 nm). In this way, differences due to point 2 are obviously removed and differences due to point 3 are minimized (the two mentioned ABL definitions are equivalent if the ABL is well-mixed, and this typically happens when the solar convective activity is relevant, i.e. when the ABLH is not minimal). Accordingly, considering only these reference points, the mean square differences are reduced considerably for the wavelengths 532 and 1064 nm, while they are almost unmodified for the 355 nm. This is a further indication that the shorter lidar wavelength is the worst performing among the available ones for the ABLH determination. Among the three considered wavelengths, the one providing the best agreement with respect to the reference is the 532 nm. Even if this wavelength is not the larger available, the better

agreement could be explained by considering that the corresponding lidar channel has a sensibly lower full overlap height with respect to the 1064 nm lidar channel. Consequently, the number of reference points above the full overlap height of the 532 nm lidar channel (16) is bigger than the number of the ones above the full overlap height of the 1064 nm lidar channel (14). The results indicate that in the best case the optimized configuration of MIPA can retrieve ABLH with a mean difference of only 3 m with a corresponding standard error of 53 m.

Tab. 4 Statistical analysis of the differences with respect to the reference of the ABLH retrieved by MIPA on high-resolution timeseries of the total attenuated backscatter at 1064, 532 and 355 nm for both the case studies considered. The mean (Δ_{mean}), the median (Δ_{med}), the standard deviation (Δ_{SD}), the standard error (Δ_{SE}), the mean square difference (Δ^2_{mean}), the minimum (Δ_{min}) and the maximum (Δ_{max}) of the differences are given in meters. N is the number of points on which the statistics are carried out. The reference is assumed to be the ABLH calculated from the co-located radiosounding data.

Table 4: Statistical analysis of the differences with respect to the reference of the ABLH retrieved by MIPA on high-resolution timeseries of the total attenuated backscatter at 1064, 532 and 355 nm for both the case studies considered.

The mean (Δ_{mean}), the median (Δ_{med}), the standard deviation (Δ_{SD}), the standard error (Δ_{SE}), the mean square difference (Δ^2_{mean}), the minimum (Δ_{min}) and the maximum (Δ_{max}) of the differences are given in meters. N is the number of points on which the statistics are carried out. The reference is assumed to be the ABLH calculated from the co-located radiosounding data.

	All reference points			Only reference points above lidar full overlap height		
	1064 nm	532 nm	355 nm	1064 nm	532 nm	355 nm
Δ_{mean} [m]	106	103	111	-120	3	22
Δ_{SD} [m]	354	282	407	198	212	426
Δ_{med} [m]	-16	19	120	-81	-82	-110
Δ_{SE} [m]	74	62	89	53	53	107
Δ_{min} [m]	-515	-227	-409	-515	-227	-409
Δ_{max} [m]	949	847	1250	216	488	1250
Δ^2_{mean} [m ²]	130842	86202	169906	50972	42085	170779
N	23	21	21	14	16	16

5. MIPA VALIDATION/OPTIMIZATION ON LPL

In this last section we describe the optimization of MIPA when applied to the observations made by the three ceilometers participating in the measurement campaign.

For the ceilometer CHM15k, we have applied MIPA on the timeseries of normalized range corrected signal provided as output by the instrument using the NetCDF variable float `beta_raw(time, range)`. This quantity is computed internally by CHM15k analysis software correcting for known instrumental effects and calibrating the range corrected signal. More details could be found in the official CHM15k documentation. No additional external processing has been made before ingesting them in MIPA as input.

For the ceilometers CL31 and CL51, MIPA has been applied on the timeseries of range corrected signals provided as output by the instrument as the L2 NetCDF product by the variable `int_profile_data(timeDim, range)`. As for the previous case no external processing has been made on such quantity before the ingestion in MIPA.

Similar to the procedure described in Sec. 5, we varied all the MIPA configuration parameters until the differences of the calculated ABLHs with respect to the corresponding reference points were minimal. The corresponding results are summarized in Tab. 5 for the three considered ceilometers.

Table 5: Optimized MIPA configuration parameters for the three wavelengths of POLPO (see Sec. 3 for the more detailed parameters description)

Parameter	Description	Optimized value		
		CHM15k	CL51	CL31
R	Input image down-sampling factor	4	6	6
P	Clipping maximum percentile	65	60	70
I_{pre}	Length of pre-processing structuring element (horizontal line along the time direction)	3	3	3
I_{post}	Length of post-processing structuring element	4	4	4
θ_{\min}	Minimum angle (with respect horizontal direction) of post-processing structuring element	-66°	-66°	-66°
θ_{\max}	Maximum angle (with respect horizontal direction) of post-processing structuring element	66°	66°	66°
δ_{post}	Euclidean distance threshold among objects and related neighborhood objects	10	10	10

Fig. 6 shows the ABLH retrieved by MIPA (red curve) when applied to the timeseries of range corrected signal of the ceilometers CHM15k, CL51 and CL31 for the case study 1 (on the left) and 2 (on the right) when the optimal values reported in Tab.5 are used. Gray dots provide the reference ABLH dataset given in Tab. 2.

Additionally, we have compared the ABLH retrieved by MIPA with the ABLH calculated by the three ceilometers using their proprietary algorithms (herein internally calculated). All the considered ceilometers provide three different candidates for the ABLH, and each of them with a corresponding quality score. Fig. 7 provides a comparison of the MIPA retrieved ABLHs against the internally calculated ABLHs by each ceilometer with the highest quality score. It is evident that on average in all the cases the ABLH provided by MIPA are in better agreement with the reference values with respect to the ABLH best estimates provided by the three ceilometers. However, especially for the two Vaisala ceilometers it seems that the ABLHs internally calculated perform better than MIPA during nighttime conditions. One of the reasons for this better agreement could be that the ceilometers use different input data (not available) from the ones considered here. Additionally, all the details of the algorithm used by the ceilometers to get ABLH is not documented.

However, it is to be pointed out that the lack of sensitivity of the MIPA algorithm within the overlap region is the result of a sensitivity lack of the lidar and/or ceilometer measurements (the number of collected backscattered photons in this region is sensitively smaller, leading to an abrupt increase of the statistical uncertainty affecting the elastic backscatter signals). Additionally, the application of the described clipping operation to reduce the dynamic range of the input image could lead to sub-optimal behaviour of the MIPA algorithm in the presence of highly variable elastic backscatter signals.

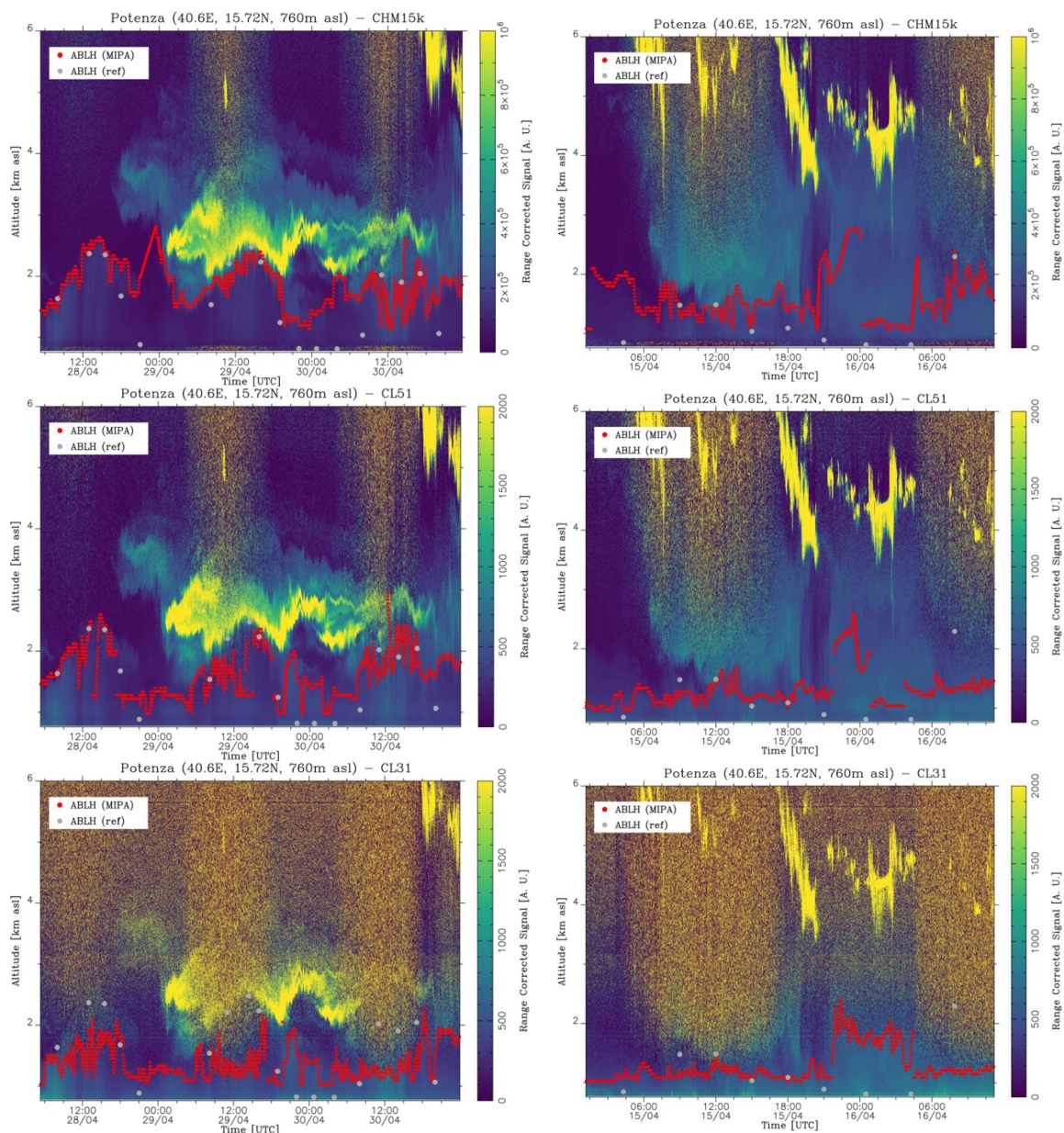


Figure 6: Case study 1 (on the left) and 2 (on the right)

range corrected signal measured by CHM15k (top row), CL51 (middle row) and CL31 (bottom row). The red curve shows the ABLH as retrieved by MIPA while the gray dots are the reference ABLH calculated from radiosoundings.

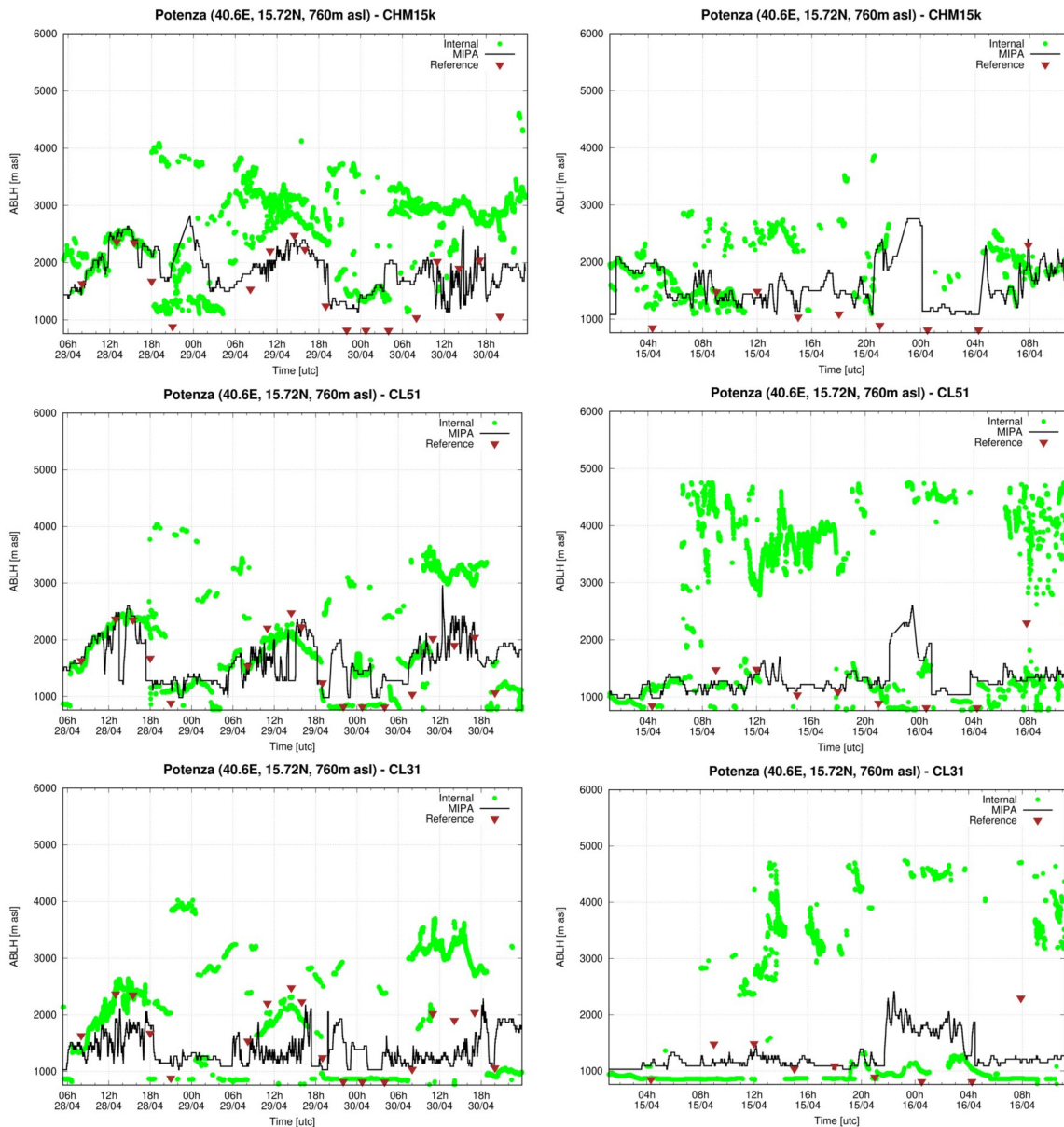


Figure 7: Case study 1 (on the left) and 2 (on the right).

ABLH calculated by MIPA (black curve) for CHM15k (top row), CL51 (middle row) and CL31 (bottom row). Green dots represent the value of ABLH with the highest quality score internally calculated by each ceilometer with proprietary algorithm. Brown triangles are the reference ABLH calculated from radiosoundings.

Finally, we summarize in Tab. 6 the statistical analysis of the differences between MIPA calculated ABLHs and corresponding reference values. Comparing these values with the corresponding ones reported in Tab. 4, ABLH retrieved by HPLs observations are more accurate than the ones retrieved by LPLs, as expected. Additionally, considering the three ceilometers the best MIPA performance is achieved by the CL51 model, followed by CHM15k and the CL31, which is the least suitable to get accurate ABLH estimations.

Tab. 6 Statistical analysis of the differences with respect to the reference of the ABLH retrieved by MIPA on timeseries of range corrected signal of ceilometers CHM15k, CL51 and CL31. The mean (Δ_{mean}), the median (Δ_{med}), the standard deviation (Δ_{SD}), the standard

error (Δ_{SE}), the mean square difference (Δ_{mean}^2), the minimum (Δ_{min}) and the maximum (Δ_{max}) of the differences are given in meters. N is the number of points on which the statistics are carried out. The reference is assumed to be the ABLH calculated from the co-located radiosounding data.

Table 6: reference points

	All reference points		
	CHM15k	CL51	CL31
Δ_{mean} [m]	325	76	-126
Δ_{SD} [m]	451	501	597
Δ_{med} [m]	262	69	-184
Δ_{SE} [m]	87	96	115
Δ_{min} [m]	-203	-1198	-1148
Δ_{max} [m]	1387	948	998
Δ_{mean}^2 [m ²]	301818	247020	358936
N	27	27	27

Even if the accuracy of the ABLH obtained by MIPA is, in general, better when the HPLs are considered, it has to be stressed that ceilometers are more widespread than the HPLs as, in general, they are cheaper devices, much less complex to operate and working 24/7. Moreover, they are characterized by smaller telescope and larger FOV allowing in principle to better investigate the atmospheric region close to the ground where especially during the nighttime measurement the ABLH is located. In this context the optimization and validation of MIPA on such sensors could really help in providing a better and continuous characterization of the ABL on large scale (like for example continental one).